Charge transfer at the metal-insulator transition in V_2O_3 thin films by resonant inelastic x-ray scattering

C. F. Hague, J.-M. Mariot, V. Ilakovac,* and R. Delaunay
Laboratoire de Chimie Physique-Matière et Rayonnement (UMR 7614), Université Pierre et Marie Curie, 11 rue Pierre et Marie Curie, 75231 Paris Cedex 05, France

M. Marsi
Laboratoire de Physique des Solides (UMR 8502), Université Paris-Sud, Bâtiment 510, 91405 Orsay Cedex, France

M. Sacchi and J.-P. Rueff
Synchrotron SOLEIL, L'Orme des Merisiers, Saint-Aubin, Boîte Postale 48, 91192 Gif-sur-Yvette Cedex, France

W. Felsch
I. Physikalisches Institut, Universität Göttingen, Friedrich-Hund-Platz 1, 37077 Göttingen, Germany
(Received 21 September 2007; revised manuscript received 20 November 2007; published 25 January 2008)

The metal-insulator transition in V_2O_3 thin films has been studied by resonant inelastic x-ray scattering (RIXS) at the V L_3 edge. Features belonging to *d-d* excitations, charge transfer between O $2p$ and V $3d$ states, and normal x-ray emissionlike decay indicate that intraband, interband, and intersite transitions are involved. In particular, our findings are compatible with a more pronounced density of unoccupied nondegenerate a_{1g} states in the paramagnetic insulator (PI) phase compared to the paramagnetic metal (PM) or antiferromagnetic insulator (AFI) phases. The O $2p$ to V $3d$ charge transfer is reduced in the PI phase compared to both the PM and AFI phases. The RIXS spectra also provide an estimate of the crystal-field splitting for V_2O_3.

DOI: 10.1103/PhysRevB.77.045132 PACS number(s): 78.70.En, 71.30.+h, 71.27.+a

I. INTRODUCTION

Though the metal-insulator transition (MIT) observed in V_2O_3 is often presented as archetypal of a Mott-Hubbard transition, it is now recognized that such a model does not fully cope with the complexity of its electronic structure. Details of its phase diagram, originally presented by McWhan *et al.*,[1] are discussed in many recent papers (see, for example, Refs. 2–5 and references therein).

Described in general terms, V_2O_3 is a paramagnetic metal (PM) above ≈155 K. There is an isostructural transition to a paramagnetic insulator (PI) phase as the V *d*-band width is reduced on expanding the lattice by substituting ≈2% Cr for V. Below ≈155 K, there is a further phase transition to an antiferromagnetic insulator (AFI), this time accompanied by a change from the rhombohedral (corundum) to a monoclinic structure whether starting from the PI or PM. Doping with Ti shrinks the lattice and increases the *d*-band width. At 5% Ti or more, the PM phase subsists even at low temperatures. In fact, spectroscopic and structural studies indicate that such a description is too simplistic. For a start, the rhombohedral structure is subject to a small trigonal distortion so that each vanadium atom is surrounded by six oxygen atoms but the t_{2g} orbitals are further split into nondegenerate a_{1g} and doubly degenerate e_g^π states. The monoclinic crystal structure has a complicated spin structure with antiferromagnetic stacking of ferromagnetic planes. Again, the t_{2g} orbitals are thought to split into nondegenerate e_g^π and a_{1g} components. The a_{1g} orbitals point along the *c* axis in the rhombohedral phase, but the e_g^π orbitals are tilted out of the *ab* plane. Moreover, in the monoclinic phase, the orbitals belonging to the V-V pairs are also slightly tilted relative to the *c* axis. It follows that hybridization between V $3d$ and O $2p$ orbitals may change significantly across the phase transitions and the single Hubbard band model may not hold. Thus, it is often postulated that the MIT mechanism may be intermediate between the Mott-Hubbard and charge-transfer (CT) models (see Ref. 2, for instance).

It is worth noting that electronic structure calculations underline the bandlike nature of the electronic structure of V_2O_3 but spectroscopies such as core-level x-ray photoelectron spectroscopy (XPS), x-ray absorption spectroscopy (XAS), and resonant inelastic x-ray scattering (RIXS) produce a more atomic-orbital picture by introducing Coulomb interactions between the core-hole and valence electrons.

In this paper, we report on RIXS experiments performed on V_2O_3 thin films at the V L_3 edge to look for excitations between *d* orbitals as well as CT excitations involving V $3d$-O $2p$ hybridization. We will see that in the case of RIXS, which is a second order optical process governed by the Kramers-Heisenberg relation,[6] both atomiclike and bandlike features are observed depending on the intersite interactions in the intermediate state of the process. The overlap of the two types of information has been extensively discussed previously by Idé and Kotani[7] and observed in $La_xSr_{1-x}TiO_3$ (Refs. 8 and 9) and in V_6O_{13} (Ref. 10), and very recently in VO_2 (Ref. 11).

V_2O_3 films were grown by epitaxy on single crystal sapphire to mimic the properties of doped V_2O_3 at various positions in the phase diagram (see Fig. 1). An advantage of films over single crystals is that the transition from the corundum to the monoclinic structure is not destructive so measurements can be repeated after a return to room temperature.

The sample preparation and experimental setup are described in Sec. II. We present the results in Sec. III, they are discussed in Sec. IV, and conclusions are drawn in Sec. V.

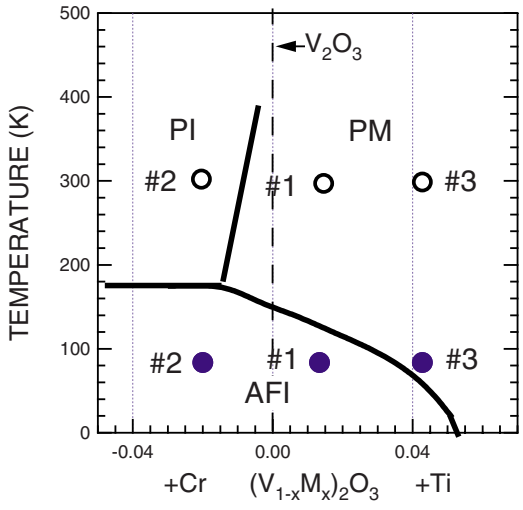

FIG. 1. (Color online) Thin film V_2O_3 samples 1 (PM), 2 (PI), and 3 (PM) at room temperature (open circles) and 83 K (filled dots) situated on a schematic representation of the temperature versus doping diagram for $(V_{1-x}M_x)_2O_3$. M is Cr or Ti.

II. EXPERIMENT

The V_2O_3 films were deposited at normal incidence onto polished single crystal sapphire substrates using reactive dc magnetron sputtering from a V metal target with 99.8% purity in an Ar-O_2 gas atmosphere. The substrates were $(11\bar{2}0)$ or (0001) oriented with a miscut below 0.2°. The substrates were preheated for 1 h at 600 °C prior to deposition at this temperature. All the films were 50 nm thick. The two substrate orientations make it possible to vary the properties of the samples and schematically assign them positions in the phase diagram shown in Fig. 1. Extensive characterization of the samples was carried out and details will be found in Refs. 12–14. X-ray diffraction pole-figure measurements reveal complete epitaxy to the substrate, without the formation of structural domains.

Specular x-ray reflectivity (Cu $K\alpha$) was used to measure thickness and roughness. Bragg reflection θ-2θ x-ray scans show that the lattice parameter for the film on the $(11\bar{2}0)$ substrate (sample 1) is similar to that of the bulk material. Resistivity measurements show a clear first-order transition with a reversible PM-AFI transition at nearly the same temperature as in the bulk material. The antiferromagnetic order in the insulating phase is reflected in the observation of magnetic exchange anisotropy in thin ferromagnetic overlayers (Fe, Co, and Ni).[13]

Sample 2 grown on the (0001)-oriented substrate under the same experimental conditions as sample 1 is subjected to considerable lateral strain and is in the PI phase at 300 K. This is in agreement with the sensitivity of the different oxide phases to external or chemical pressure reported in Ref. 1. Its resistance is 2 orders of magnitude higher than that of sample 1 and increases with decreasing temperature, with a steep rise across the PI to AFI transition. Film growth on the (0001) surface of sapphire at a somewhat higher partial pressure of oxygen (sample 3) reduces the strain and induces the PM phase at 300 K. The resistance is the same as that of sample 1 and shows a similar decrease toward low temperature, but has no well defined transition to an AFI phase. Below ≈150 K, electrical conduction becomes thermally activated, more in line with a semiconducting behavior with low activation energy. At 83 K (our low temperature working value), the resistance ratio, referred to the room temperature value $R_{300\ \mathrm{K}}$, is $R/R_{300\ \mathrm{K}} \approx 2$. This compares to $R/R_{300\ \mathrm{K}} \approx 10^6$ at 83 K for both samples 1 and 2. Scanning tunneling and atomic force microscopy measurements shed light on the origin of the differences in the properties of the V_2O_3 films if deposited on $(11\bar{2}0)$ or (0001) sapphire. For $(11\bar{2}0)$ orientation, self-organized growth leads to facets oriented perpendicular to the c axis which is in the film plane (sample 1). This reduces the anisotropic misfit to the substrate and leads to films free of strain. The overall root-mean-square (rms) roughness is ≈1 nm. In contrast, the (0001) surface is very flat, with rms comparable to that of the substrate (<0.14 nm) and without a preferred orientation in its morphology (samples 2 and 3).

The experiments were performed using a soft x-ray grating spectrometer[15] installed on the U41-PGM beamline at BESSY II (Berlin). The beam focus had a Gaussian shape with a 13 μm full-width at half-maximum in the vertical plane for a monochromator exit slit set to 40 μm. The Petersen-type monochromator was set to a resolving power of approximately 2000.[16]

A high-precision liquid-nitrogen-cooled xyz-θ manipulator positioned the samples to intercept the beam at the focal point. The spectrometer's optical axis was also set to intercept the best focus at the sample position, switching from one sample to the next was done by moving the sample holder vertically (z) only. All spectra were recorded 90° to the beam direction with a horizontal acceptance of ≈4°. In this geometry, elastic scattering was minimized because the polarization vector of the linearly polarized incident photons was in the scattering plane. The samples were placed at ≈25° grazing angle relative to the beam. Thus, excitations involving orbitals in the c-axis direction should be emphasized over the roughly in-plane e_g^π states for samples deposited on (0001) sapphire, while the e_g^π orbitals would be emphasized for sample 1 on $(11\bar{2}0)$. We will see that this helps to interpret our data when room temperature measurements on samples 1 and 3 are compared. The film thickness of 50 nm is comparable to the attenuation length of the incident radiation in the sample above the V $L_{2,3}$ edge.[17] Thus, the x-ray emission signal relates reliably to the resistance measurements. Because of the limited thickness of the samples, the O K emission from the sapphire substrate will contribute, though weakly because of self-absorption, to the RIXS oxygen signal. RIXS measurements were performed at ≈300 K and 83 K.

The soft x-ray grating spectrometer was operated in a slitless mode. This meant that the beam spot size limited the resolution to ≈0.7 eV. A slitless operation has the advantage that the spectrometer acceptance angle is optimized. Thus, satisfactory statistics were obtained with short accumulation times. In practice, all the RIXS data shown in the figures were the sum of two 10 min acquisition times at storage ring currents ranging from 250 to 125 mA. Thus, it was possible

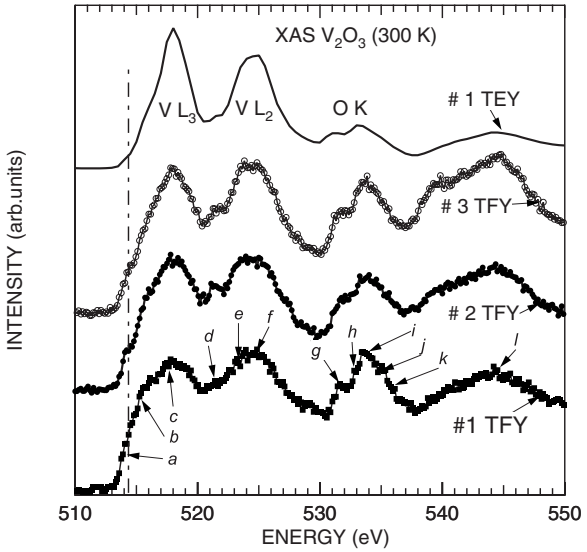

FIG. 2. V $L_{2,3}$ and O K XAS obtained by TFY for V_2O_3: Sample 1, PM on $(11\bar{2}0)$ sapphire; sample 2, PI; and sample 3, PM on (0001) sapphire. The TEY spectrum for sample 1 is also shown.

to collect about 30 pairs of spectra covering a range of excitation energies, at two temperatures within a 12 h period. This was important because the beamline is shared and operates in alternate-user 12 h shifts. It meant that reliable comparisons could be made without the need for elaborate recalibrations after each change of user.

The spectrometer operates in a flat-field mode with the detector set perpendicularly to the direction of the collected photons. We used a 25 mm diameter microchannel plate (MCP) to record XAS in the total fluorescence yield (TFY) mode with the spectrometer set at zero order. It was also used to record x-ray emission spectra (XES) over a broad energy range. In these measurements, the MCP's spatial resolution of ≈ 80 μm limits the observable energy resolution. The RIXS data were recorded over a more limited energy range with a charge coupled device with 13×13 μm^2 pixels. Here, the size of the beamline focus is the limiting factor. Except where otherwise stated all spectra are presented normalized to the same accumulation time and average storage ring beam current. The values of the incident photon energies were taken as given by the U41-PGM monochromator; they differ by $\approx +1.3$ eV compared to the energy scale reported by Park *et al.* for their XAS $(V_{1-x}Cr_x)_2O_3$ data.[18] The spectrometer was calibrated against the U41-PGM values by observing elastically scattered peaks. The monochromator uses the N $1s \rightarrow \pi^*$ resonance in N_2 as a reference point for the energy scale.

III. RESULTS

A. X-ray absorption spectroscopy and overview of x-ray emission spectra

The room temperature XAS spectra are presented in Fig. 2. The incident photon energy resolution (≈ 0.25 eV) was the same as that used in the RIXS experiments. TEY measurements at other temperatures have already been reported for similar samples[12] and therefore were not repeated here. The quality of the TFY data was limited by the low counting rate through the spectrometer but the spectra show the main features of the more surface-sensitive TEY method. The room temperature thin film TEY spectrum is in good agreement with its analog recorded by Park *et al.*[18] for a single crystal. The TFY signal shows a slightly sharper step at 515.2 eV in the PI (sample 2) compared to the two PM samples in qualitative agreement with the observation by Park *et al.* The differences between the TFY and TEY measurements are largely attributable to self-absorption.

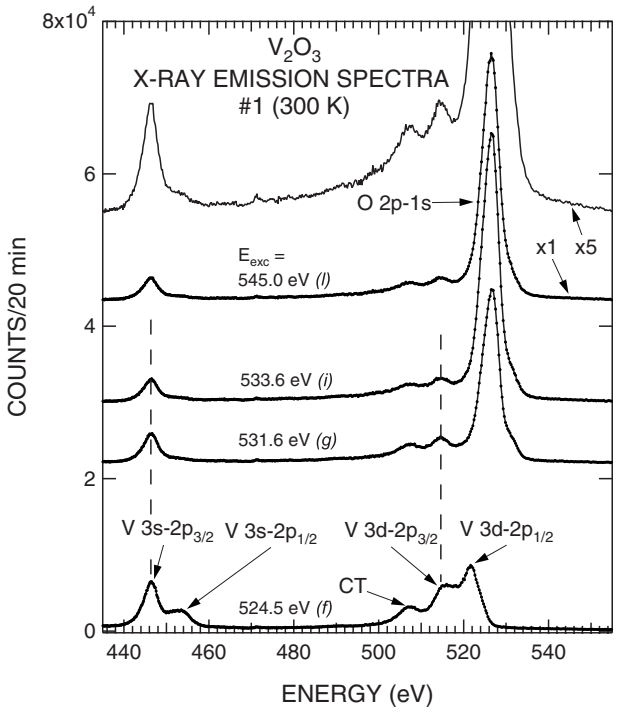

FIG. 3. Extended energy range with limited resolution showing V $2p$ and O $1s$ XES in V_2O_3 (sample 3) to include valence band region and the V $3s$-$2p$ core lines. The V $3s$-$2p_{1/2}$ line is attenuated by Coster-Kronig transitions except at the $2p_{1/2}$-$3d$ resonance. Letters refer to points on the XAS curves (Fig. 2).

In Fig. 2, the main features of interest are identified by lower-case letters in Fig. 2. Features a, b, and c in the V L_3 part of the spectrum at 513.8, 515.2, and 517.6 eV, respectively, are those we concentrate on in this paper. Similar features roughly 7–8 eV higher in energy are also observed at the V L_2 part of the spectrum.

In Fig. 3, we present an overall view of the V $3d$-$2p$ and O $2p$-$1s$ x-ray emission spectra and include the V $3s$-$2p$ emission lines taken with the MCP. Four curves are plotted for incident photon energies (E_{in}) tuned to f, g, i, and l on the XAS curves (V L_2 peak, onset of O K edge, O K absorption peak, and well above O K threshold, respectively). It is instructive to note that the V $3s$-$2p_{1/2}$ emission line is almost completely suppressed by the $L_2-L_3M_{4,5}$ Coster-Kronig transition except when E_{in} is tuned to the L_2 absorption maximum. Thus, the V $3d$-$2p_{1/2}$ fluorescence emission, weakened by the Coster-Kronig transition, contributes very little to the intensity of the low energy tail of the O K emission band. On the other hand, there is some overlap between

the L_2 and L_3 features because V $3d$-O $2p$ hybridization gives rise to a band separated in energy from the main V $3d$ band by about the same value as the spin-orbit splitting. This explains why we concentrate on measurements at the V L_3 edge.

The x-ray fluorescence regime, also known as normal x-ray emission (NXE), occurs when E_{in} is set well above the V $L_{2,3}$ or O K thresholds. The NXE peak observed at 514 eV corresponds to the V $3d$-$2p_{3/2}$ transition. Setting aside electron correlations and many-body effects, it may be compared to the peak observed close to the Fermi energy (E_F) by XPS (Ref. 5) and to the electronic structure calculations using the density functional theory within the local density approximation (LDA) by Mattheiss[20] which situate the $3d$-projected occupied density of states within 1 eV of E_F. The 507 eV emission band corresponds to mainly O $2p$ states hybridized with V $3d$ states. Its equivalent in XPS is a broad band at a binding energy of ≈6 eV. The LDA calculation also situates the O $2p$ band ≈6 eV below E_F.

B. Resonant inelastic x-ray scattering: Paramagnetic phases

Figure 4 shows a data set for sample 1 in the PM phase at various incident photon energies up to the V L_2 absorption maximum and across the O K edge. Both are plotted as a function of emitted photon energy. Room temperature RIXS has been reported by Schmitt *et al.*[21] for a single crystal of V_2O_3. It appears that at room temperature, at least, our thin film samples are closely similar to the crystalline material. We note, at first glance, that all the spectra show peaks at 507 and 514 eV as though structure at these emitted photon energies were independent of the excitation energy and consistent with NXE. As we will see, this does not necessarily rule out the presence of RIXS features at those energies. Figure 5 shows the evolution of the V $2p3d$ RIXS for sample 2 in the PI phase as E_{in} is scanned across the V L_3 edge from 512.8 to 517.6 eV. From here on, we trace the spectra on an energy transfer scale ($E_{in}-E_{out}$), i.e., relative to the excitation energy. Plotting spectra in this way helps identify x-ray Raman features as they remain at constant energy transfer. NXE-like features, on the contrary, disperse as E_{in} is increased.

The first resonance corresponds to the elastic peak on reaching 513.8 eV (a). The elastic peak is asymmetric suggesting the presence of unresolved structure at an energy loss ranging down to ≈−2 eV. The next inelastic resonance, A, appears at E_{in}=515.2 eV and is observed at ≈−1.8 eV. This results from a d-d excitation. The other main feature, C, is a broad band at ≈−7 eV in the E_{in}=513.8 eV spectrum; it corresponds to a CT excitation where an electron has been transferred from the O $2p$ band into V $3d$ orbitals in the final state. In terms of a configuration interaction model, this energy loss corresponds to an excitation from the ground state to $3d^{n+1}\underline{L}$ ($\underline{L}$ indicates a ligand hole). It involves a $2p^5 3d^{n+1}$ intermediate state. This peak disperses as from E_{in} ≈514 eV. A further peak, B, is well resolved at E_{in} =517.6 eV corresponding to excitation to peak c in the XAS curve. We will see below that changes in the RIXS data as a function of sample and sample temperature are small, as indeed those observed by XAS (Refs. 12 and 18) but of significance when trying to determine the changes in electronic structure driving the phase transitions.

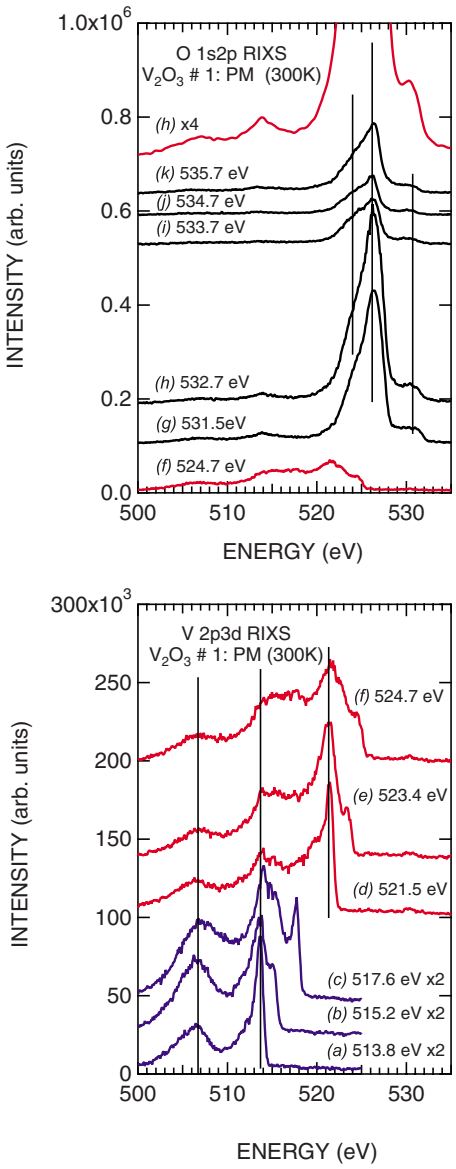

FIG. 4. (Color online) RIXS spectra recorded across the V $L_{2,3}$ (lower panel) and O K (upper panel) absorption edges. The letters relate to the energy values of Fig. 2. Curve h is presented on an expanded intensity scale to show the V $3d$ fluorescence spectrum. Here and in the following figures, the experimental resolution is ≈0.7 eV

C. Resonant inelastic x-ray scattering: Temperature dependence

1. 513.8 eV excitation

The low temperature measurements performed for an excitation to a on the XAS curve show a stronger elastic peak for samples 1 and 2 compared to the room temperature measurements; for sample 3, no change is observed to within the experimental precision (see Fig. 6). The observation of an

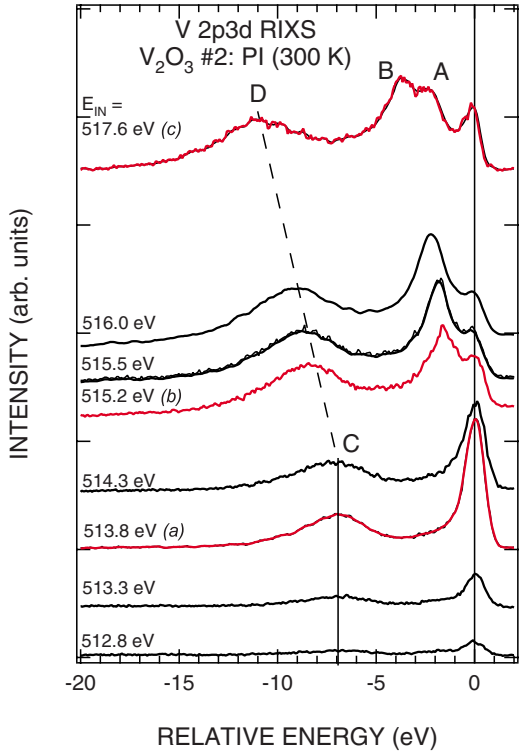

FIG. 5. (Color online) V $2p3d$ RIXS spectra recorded across the V $L_{2,3}$ edge on an energy transfer scale ($E_{in}-E_{out}$). The spectra are offset proportionally to E_{in}.

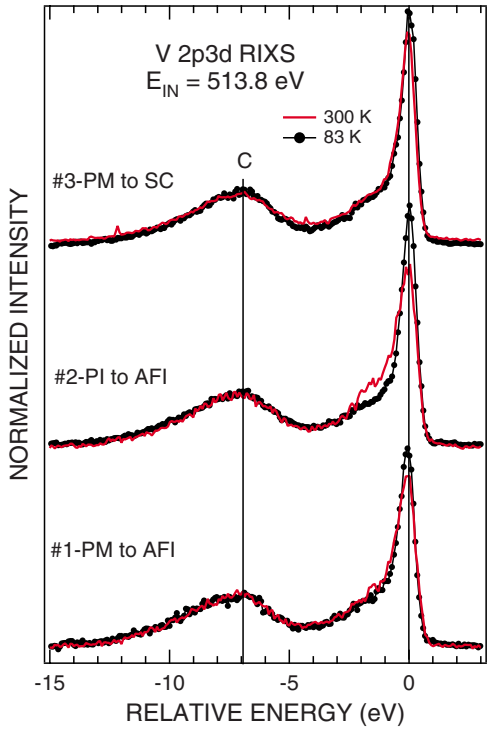

FIG. 6. (Color online) V $2p3d$ RIXS recorded at E_{in} =513.8 eV (*a* in Fig. 2) at room temperature and at 83 K.

elastic component even at a 90° scattering angle has been explained by Matsubara *et al.*,[19] who showed that the dipole selection rule gives nonzero elastic intensity in the case of $3d^1$ and $3d^2$ systems. They used a cluster model in which the metal atom is surrounded by six ligand atoms in O_h symmetry.

The increase in the intensity of the elastic peak at low temperature is most likely the consequence of the magnetic ordering in the AFI phase which introduces a rotation of the incident beam polarization vector. In the figure, each pair of high and low temperature spectra has been normalized to the same total intensity to search for changes in shape. The loss structure shows a small increase in intensity for the PI phase, though not well resolved. We attribute this structure to a *d-d* excitation. The strong CT band C observed at −7 eV is identical for all the spectra at this value of E_{in}.

2. 515.2 eV excitation

Figure 7 shows data taken close to the second resonance (*b* in Fig. 2) which consists of a main *d-d* excitation at ≈−1.7 eV and an O $2p$-related peak at −8.5 eV. Small shifts are apparent (Fig. 7, right panel) between the room temperature and low temperature spectra. At 300 K, the *d-d* peak is stronger for sample 1 than for sample 3 although they are both in the PM phase. We attribute this to the difference in *c*-axis orientation relative to the incident photon polarization vector (see discussion below). In view of the sharp relatively simple resonance, these spectra can be fitted quite reliably by Gaussian line shapes to help identify the changes. For clarity, we only show one set of fits in Fig. 7 (83 K spectrum for sample 2). For all three samples, the *d-d* transition gives a peak at −1.65 eV at 83 K. At room temperature, the peak shifts to −1.5 eV for the two metallic samples and to −1.2 eV for the PI phase. The semiconductor low temperature spectrum shows a stronger *d-d* peak at −1.9 eV. The *d-d* excitation extends to ≈−3 eV. From the fitting procedure to take into account the modification in the position of the energy-loss peak closest to E_F, it is found that the amplitude of the elastic peak increases in the AFI phase.

3. 517.6 eV excitation

The spectra taken with E_{in} tuned to peak *c* in the V L_3 XAS are shown in Fig. 8. Other than the elastic peak, there are three main features at −2.1, −3.6, and −10.4 eV (A, B, and D, respectively). The *d-d* part of the band is somewhat complex with a change in the relative intensity of A and B when going from room temperature to low temperatures. Fitting the data with Gaussian peaks is not unequivocal so such a procedure cannot contribute constructively to explaining the origin of the structure. Even so, we note that at least three peaks are needed to simulate this *d-d* part of the spectrum. Thus, to discuss the changes observed, we take advantage of the good statistics (the overall fit leaves very small residuals) by taking the differences between fits to the 517.6 eV spectra (the most marked difference is for the transition from PI to AFI, see Fig. 8, top panel). The elastic peak amplitude is again reduced by ≈8% on going from the magnetically ordered AFI phase to the PM and PI phases. No such change is observed as a function of temperature for sample 3. Peak B in the room temperature phases coincides with a small dip in

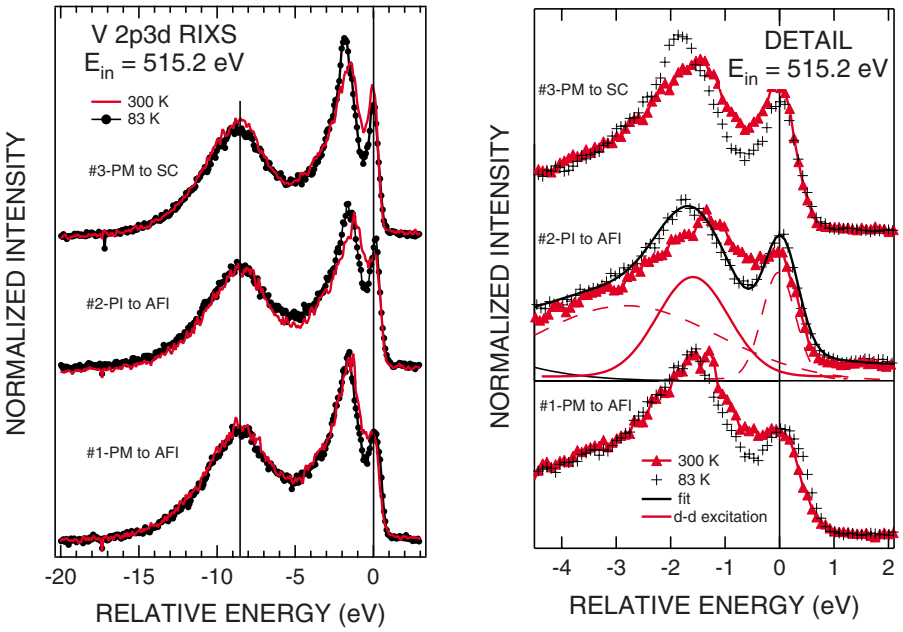

FIG. 7. (Color online) V $2p3d$ RIXS recorded at E_{in}=515.2 eV (*b* in Fig. 2) at room temperature and 83 K. The *d-d* transition part of the same data is shown on an expanded energy scale (right panel). For clarity the Gaussian fits are shown for sample 2 AFI phase only.

the AFI spectra. A significant change in intensity is observed for the *d-d* part in the region extending from −3.6 to −1.8 eV and also at −7 eV. We note that the intensity of peak B drops also in sample 3. The implications are discussed in the next section.

IV. DISCUSSION

The LDA calculations by Mattheiss[20] mentioned above provide a good overall parameter-free description of the interactions between V $3d$ and O $2p$ states in V_2O_3 but leave out the crucial correlation effects which lead to the metallic state and the narrow gap PI phase. However, they serve as a sound basis for calculations into which the electron correlation energy U (Hubbard U) can be introduced. LDA+U calculations to describe the PM-AFI transition were first implemented by Ezhov *et al.*[22] who took into account the actual AFI monoclinic crystal structure. They concluded that the ground state is two parallel spin electrons in e_g^{π} in accordance with Hund's rule leaving a_{1g} essentially empty. More recently, Elfimov *et al.*[23] using a tight-binding fit to LDA +U and downfolding techniques showed that, though the spatial orientation of the a_{1g} orbitals are indeed favorable to hopping between molecularlike V pairs along the *c* axis as proposed by Castellani *et al.*,[24] other interactions need to be taken into account. They concern hopping between more distant V atoms making the likelihood of orbital ordering with a filled a_{1g} ground state unlikely.

Over the past decade, the development of dynamic mean-field theory (DMFT) (see, for instance, Ref. 25) has also been driven, to a large extent, by interest in the MIT in transition metal compounds. Applied specifically to high energy XPS experiments, it is able to explain the temperature dependence of the quasiparticle (QP) peak in the valence band of the PM $(V_{1-x}Cr_x)_2O_3$ (Ref. 5) and V_2O_3 (Ref. 26). The V $2p$ XPS spectrum is also interesting because it too shows a QP peak in the form of a shake-down satellite. It shows that the V $2p$ core-hole final state with an electron removed is strongly screened by the QP peak in the PM phase[27] but disappears at the transition to the AFI phase.[26] Very recently, Poteryaev *et al.*[28] have studied the PM to PI transition using DMFT allied to LDA (see also Ref. 29). Their study shows that the coherence scale depends strongly on the orbital structure and they confirm that the a_{1g} band is almost empty (the a_{1g} occupancy drops when going from the PM to PI phase). This in turn has implications for the bandwidth and low energy hybridization.

To date, multiplet calculations are the only tractable approach to describing RIXS spectra,[6] but none are available for V_2O_3. As mentioned in Sec. III C, calculations have been performed on VF_3 by Matsubara *et al.*,[19] and though the electronic structure of these compounds differ, both are nominally $3d^2$ systems, so a comparison provides some insight into the main features of V_2O_3 RIXS.

To start with it is instructive to compare our V_2O_3 data with the Ti $2p3d$ RIXS experiments performed by Higuchi *et al.*[8,9] on $La_xSr_{1-x}TiO_3$ which at x=0 is a Mott-Hubbard insulator, while at x=1, it is a band gap insulator and at values in between, it has a PM phase.

We saw above that excitation to the main absorption peak *c* for V_2O_3 results in a double structure in the RIXS spectrum at −2.1 and −3.6 eV labeled A and B, respectively (see Fig. 5). Similarly, RIXS resulting from the excitation to the main Ti L_3 absorption peak shows a double peak situated at −1.6 and −2.8 eV. The −1.6 eV peak is attributed to a transition from the Ti-O t_{2g} orbital to the unoccupied e_g orbitals, thus to the $10Dq$ crystal-field splitting. The other peak is attributed to NXE as it coincides with the main peak in the Ti $2p$ fluorescence spectrum. Reasoning along the same lines, $10Dq$ for V_2O_3 would be 2.1 eV and peak B at −3.6 eV would correspond to the V $3d$-$2p$ NXE peak which lies at 514 eV on a scattered-photon energy scale. Our experimental value for $10Dq$ is larger than the value of 1.8 eV assumed by Mossanek and Abbate[30] for their cluster model calculation for V_2O_3.

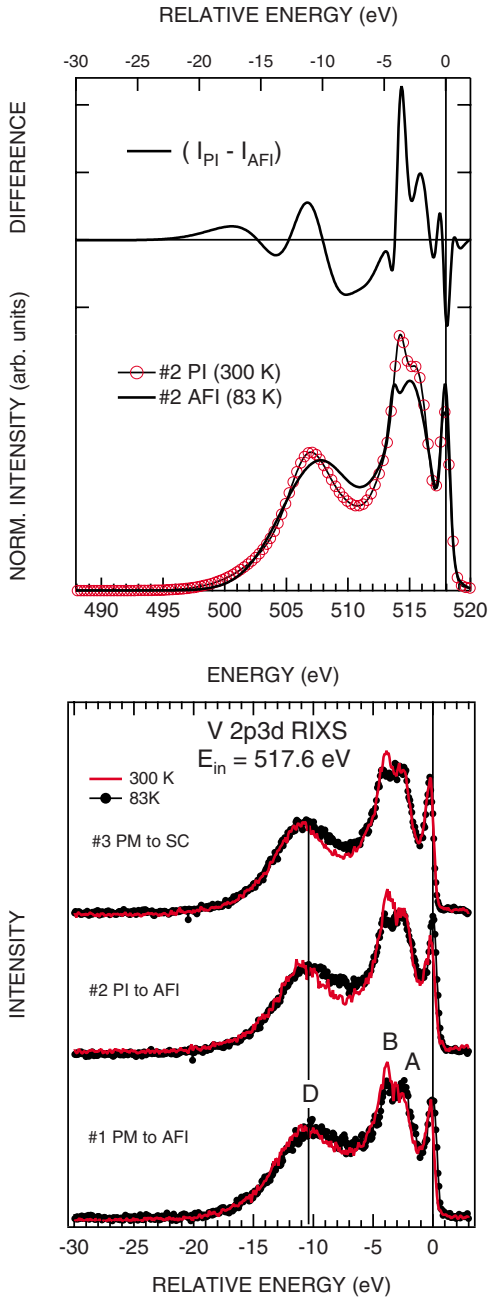

FIG. 8. (Color online) V $2p3d$ RIXS recorded at E_{in} =517.6 eV (c in Fig. 2) at room temperature and 83 K (bottom panel). Also shown is the difference between PI and AFI spectra (top panel). The difference between fitted curves is used for better clarity.

On the other hand, by analogy with the VF_3 multiplet calculations,[19] peak B might be assigned to a d-d excitation. In VF_3, the antibonding $2p^53d^{n+2}\underline{L}$ states are shown to form the main peak of the calculated XAS spectrum which is broadened by the multiplet coupling between $3d$ electrons as well as between the ligand and V $3d$. Excitation to these antibonding states leads to peaks at −1.8 and −3.4 eV in the RIXS spectrum, i.e., close to the values we observe for V_2O_3. The calculations show no energy-loss structure close to the elastic peak at the onset of the V $2p$ edge ($2p^53d^{n+1}$ intermediate state). This is also the case for the V_2O_3 experimental spectra except for the asymmetry of the elastic peak, which, here, may be attributed to energy loss structure involving the nondegenerate t_{2g} states. Calculations for E_{in} ≈515.2 eV, where we observe a single strong loss peak at ≈−1.6 eV, are not reported. Matsubara *et al.*[19] also point out that the CT peak in VF_3 situated at −7 eV for an excitation to $2p^53d^{n+1}$ shifts by −3 eV when the excitation is to the absorption maximum. However, assigning peak D (see Fig. 7) to CT, as opposed to an NXE-like structure, remains somewhat problematic because of the more metallic character of V_2O_3.

The equivalent to peak A in the $La_xSr_{1-x}TiO_3$ experiments is a fairly symmetric peak at ≈−2.0 eV. The latter involves the unoccupied part of the t_{2g} states and is attributed to a transition from the lower Hubbard band to the unoccupied coherent QP band. In the case of the Ti d-d transition, the intensity decreases in the metallic phase. For V_2O_3, the peak shifts towards the elastic peak when going from the PM to PI phase but remains at practically the same energy for the AFI phase. The different behavior arises from the greater complexity of the t_{2g} band in V_2O_3 (mixing of e_g^π, e_g^π and e_g^π, a_{1g} states) and the stronger interaction of the antibonding (cubic) e_g^σ states with e_g^π as compared to a_{1g} orbitals. Support for this comes from the XAS data and LDA results: at the Ti L_3 edge, t_{2g} and e_g are separated into two well defined peaks, whereas in V_2O_3, the t_{2g} states appear as a shoulder to the main absorption peak. Mattheiss[20] noted that according to his LDA calculations, the E_g orbitals, i.e., the e_g^σ states, were more strongly mixed with the orbitals forming the π-type bond than those lying along the c-axis direction.

Excitation to the e_g^π states is expected to be reinforced for sample 1 compared to sample 3 because of the c-axis orientation imposed by the orientation of the sapphire substrate. This is indeed what we observe for the 515.2 eV spectra. The final state of the RIXS process gives rise to lower energy-loss structure for PI than for the other phases. This suggests excitation to more localized a_{1g} states, whereas PM and AFI V_2O_3 show a shift to higher energy loss with the center of gravity of the d-d transition moving toward the more delocalized e_g^σ states. From their XAS multiplet calculations, Park *et al.*[18] concluded that the a_{1g} occupation was highest in the PM and lowest in the PI phase. The details of this process are of course different as concerns the PM and AFI phases. In the former, excitation to the QP band would be partially masked by the stronger band dispersion resulting from the t_{2g}-e_g interaction, while in the latter, the opening of the band gap to ≈0.6 eV contributes to the larger energy loss. The weak energy-loss structure observed for excitations at the onset of the XAS (513.8 eV) can be attributed to d-d transitions within the nondegenerate t_{2g} orbitals involving QP states in the sense that going from the metallic to the PI phase would transfer spectral weight into the upper Hubbard band explaining that we see a small increase in the RIXS intensity. Again, that the PM and AFI spectra differ from the PI phase, yet are similar, does not necessarily imply that their electronic structure is similar. Better resolving power would likely help reveal more information in this respect.

Concerning the CT structure, we noted that the −7 eV band C dispersed to −10.5 eV as E_{in} was increased from 514 to 517.6 eV indicating an NXE-like spectrum which

represents the O $2p$ density of states via their hybridization with V $3d$ states.

Using the difference spectra (upper panel of Fig. 8) as a guide, we can identify some significant changes across the phase transitions. Other than the change in the intensity at ≈ -2.5 eV when going from PI to PM and PI to AFI phases in the d-d energy-loss region, there is a large change in the CT structure such that at -7 eV the intensity is stronger in the AFI and PM phases than in the PI phase. The dip in intensity at -7 eV is also seen in the low temperature semiconductor phase of sample 3 though it is less marked than in the PI phase. Braicovich *et al.*[11] reporting similar results for the insulating phase of VO_2 point out that the RIXS technique is intrinsically more appropriate to studies on insulating phases rather than metallic phases of transition-metal oxides. This is because of the difficulty of dealing with the overlap of NXE-like features and Raman features such as the d-d excitations. Here, we see that the changes across the phase transitions are small but worth observing in detail even as they occur into the metallic phase, because the small modifications in the hybridization are a clue to electronic-structure origin of the phase transitions.

V. CONCLUSIONS

RIXS experiments provide details of the interaction between the V $3d$ and O $2p$ states not available by other techniques. In particular, the V $2p3d$ RIXS selects the $3d$-projected spectral functions even at energies dominated by the occupied and unoccupied O $2p$ bands. Because the core-hole correlation effects appear only in the intermediate state (XAS final state), it is likely that these findings are of relevance to the electronic origin of the V_2O_3 phase transitions resulting from the strong overlap between V $3d$ and O $2p$ states. From our observations, we find that the V-O interactions are different across the PI to PM phase transition from those across the AFI to PM transition. Above all, the PI to PM transition is not solely dependent on the details of the nondegenerate $3d$ band but also involves a significant change in the CT excitation. We interpret the results as indicating that as the a_{1g} occupancy diminishes in the PI phase, d-d transitions show a lower energy-loss peak. This is accompanied by stronger interaction between the e_g^{π} states and the cubic e_g^{σ} states. As E_{in} reaches the e_g^{σ} unoccupied band, the excited electron can more readily move to neighboring atoms on the time scale of the RIXS decay process resulting in a relatively stronger NXE-like $3d$-$2p$ transition involving occupied V $3d$-O $2p$ hybridized states.

Future progress in obtaining higher resolution RIXS spectra will certainly help refine our understanding of the MIT, though in the case of materials such as V_2O_3, band dispersion is likely to interfere with the observation of significantly more detail. Model calculations along the lines of those implemented to deal with XPS and inverse photoemission[28] would certainly add insight to the experimental results, but the need to deal with the Coulomb interactions in the core-hole intermediate state as well as the long range solid state interactions is a difficult challenge.

ACKNOWLEDGMENTS

We are grateful to the BESSY II staff and, in particular, to C. Jung and M. Mast for their expertise in focusing the beam at U41-PGM, and to S. Eisebitt for stimulating discussions. Financial support for building the x-ray spectrometer was provided by LURE (Option I). M.M. would like to thank the CNRS for support during his stay at LCP-MR. This work was supported by the European Community-Research Infrastructure Action under the FP6 "Structuring the European Research Area" Programme (through the Integrated Infrastructure Initiative "Integrating Activity on Synchrotron and Free Electron Laser Science," Contract No. R II 3-CT-2004-506008).

*Permanent address: Université de Cergy-Pontoise, 95301 Cergy-Pontoise Cedex, France.

[1] D. B. McWahn, A. Menth, J. P. Remeika, W. F. Brinkman, and T. M. Rice, Phys. Rev. B **7**, 1920 (1973).
[2] A. Tanaka, J. Phys. Soc. Jpn. **71**, 1091 (2002).
[3] S. DiMatteo, N. B. Perkins, and C. R. Natoli, Phys. Rev. B **65**, 054413 (2002).
[4] M. S. Laad, L. Craco, and E. Müller-Hartmann, Phys. Rev. B **73**, 045109 (2006).
[5] S.-K. Mo, H.-D. Kim, J. D. Denlinger, J. W. Allen, J.-H. Park, A. Sekiyama, A. Yamasaki, S. Suga, Y. Saitoh, T. Muro, and P. Metcalf, Phys. Rev. B **74**, 165101 (2006).
[6] A. Kotani and S. Shin, Rev. Mod. Phys. **73**, 203 (2001).
[7] T. Idé and A. Kotani, J. Phys. Soc. Jpn. **69**, 1895 (2000).
[8] T. Higuchi, T. Tsukamoto, M. Watanabe, M. M. Grush, T. A. Callcott, R. C. Perera, D. L. Ederer, Y. Tokura, Y. Harada, Y. Tezuka, and S. Shin, Phys. Rev. B **60**, 7711 (1999).
[9] T. Higuchi, D. Baba, T. Takeuchi, T. Tsukamoto, Y. Taguchi, Y. Tokura, A. Chainani, and S. Shin, Phys. Rev. B **68**, 104420 (2003).
[10] T. Schmitt, L.-C. Duda, M. Matsubara, M. Mattesini, M. Klemm, A. Augustsson, J.-H. Guo, T. Uozumi, S. Horn, R. Ahuja, A. Kotani, and J. Nordgren, Phys. Rev. B **69**, 125103 (2004).
[11] L. Braicovich, G. Ghiringhelli, L. H. Tjeng, V. Bisogni, C. Dallera, A. Piazzalunga, W. Reichelt, and N. B. Brookes, Phys. Rev. B **76**, 125105 (2007).
[12] B. Sass, C. Tusche, W. Felsch, N. Quaas, A. Weismann, and M. Wenderoth, J. Phys.: Condens. Matter **16**, 77 (2004).
[13] B. Sass, C. Tusche, W. Felsch, F. Bertran, F. Fortuna, P. Ohresser, and G. Krill, Phys. Rev. B **71**, 014415 (2005).
[14] B. Sass, S. Buschhorn, W. Felsch, D. Schmitz, and P. Imperia, J. Magn. Magn. Mater. **303**, 167 (2006).
[15] C. F. Hague, J. H. Underwood, A. Avila, R. Delaunay, H. Ringuenet, M. Marsi, and M. Sacchi, Rev. Sci. Instrum. **76**, 023110 (2005).
[16] H. Petersen, C. Jung, C. Hellwig, W. B. Peatman, and W. Gudat,

Rev. Sci. Instrum. **66**, 1 (1995).
[17] The attenuation length is comparable to the film thickness above the V $L_{2,3}$ edge. It is shorter for excitations to peak absorption.
[18] J.-H. Park, L. H. Tjeng, A. Tanaka, J. W. Allen, C. T. Chen, P. Metcalf, J. M. Honig, F. M. F. de Groot, and G. A. Sawatzky, Phys. Rev. B **61**, 11506 (2000).
[19] M. Matsubara, T. Uozumi, A. Kotani, Y. Harada, and S. Shin, J. Phys. Soc. Jpn. **71**, 347 (2002).
[20] L. F. Mattheiss, J. Phys.: Condens. Matter **6**, 6477 (1994).
[21] T. Schmitt, L.-C. Duda, A. Augustsson, J.-H. Guo, J. Nordgren, J. E. Downes, C. McGuinness, K. E. Smith, G. Dhalenne, A. Revcolevschi, M. Klemm, and S. Horn, Surf. Rev. Lett. **9**, 1369 (2002).
[22] S. Yu. Ezhov, V. I. Anisimov, D. I. Khomskii, and G. A. Sawatzky, Phys. Rev. Lett. **83**, 4136 (1999).
[23] I. S. Elfimov, N. A. Skorikov, V. I. Anisimov, and G. A. Sawatzky, Phys. Rev. Lett. **88**, 015504 (2001).
[24] C. Castellani, C. R. Natoli, and J. Ranninger, Phys. Rev. B **18**, 4945 (1978); **18**, 4967 (1978); **18**, 5001 (1978).
[25] A. Georges, G. Kotliar, W. Krauth, and M. Rozenberg, Rev. Mod. Phys. **68**, 13 (1996).
[26] G. Panaccione, M. Altarelli, A. Fondacaro, A. Georges, S. Huotari, P. Lacovig, A. Lichtenstein, P. Metcalf, G. Monaco, F. Offi, L. Paolasini, A. Poteryaev, M. Sacchi, and O. Tjernberg, Phys. Rev. Lett. **97**, 116401 (2006).
[27] M. Taguchi, A. Chainani, N. Kamakura, K. Horiba, Y. Takata, M. Yabashi, K. Tamasaku, Y. Nishino, D. Miwa, T. Ishikawa, S. Shin, E. Ikenaga, T. Yokoya, K. Kobayashi, T. Mochiku, K. Hirata, and K. Motoya, Phys. Rev. B **71**, 155102 (2005).
[28] A. I. Poteryaev, J. M. Tomczak, S. Biermann, A. Georges, A. I. Lichtenstein, A. N. Rubtsov, T. Saha-Dasgupta, and O. K. Andersen, Phys. Rev. B **76**, 085127 (2007).
[29] K. Held, G. Keller, V. Eyert, D. Vollhardt, and V. I. Anisimov, Phys. Rev. Lett. **86**, 5345 (2001); G. Keller, K. Held, V. Eyert, D. Vollhardt, and V. I. Anisimov, Phys. Rev. B **70**, 205116 (2004).
[30] R. J. O. Mossanek and M. Abbate, Phys. Rev. B **75**, 115110 (2007).